colloids and interfaces

MDPI

Article

Electroosmotic Flow in Free Liquid Films: Understanding Flow in Foam Plateau Borders

Abdulkadir Hussein Sheik, Anna Trybala, Victor Starov and Himiyage Chaminda Hemaka Bandulasena *

Department of Chemical Engineering, Loughborough University, Loughborough LE11 3TU, UK; A.Hussein-Sheik@lboro.ac.uk (A.H.S.); A.Trybala@lboro.ac.uk (A.T.); V.M.Starov@lboro.ac.uk (V.S.)

* Correspondence: H.C.H.Bandulasena@lboro.ac.uk; Tel.: +44-(0)-1509-222515

Received: 12 January 2018; Accepted: 26 February 2018; Published: 28 February 2018

Abstract: Liquid flow in foams mostly proceeds through Plateau borders where liquid content is the highest. A sufficiently thick (~180 μm) free liquid film is a reasonable model for understanding of electrokinetic phenomena in foam Plateau borders. For this purpose, a flow cell with a suspended free liquid film has been designed for measurement of electrokinetic flow under an imposed electric potential difference. The free liquid film was stabilised by either anionic (sodium lauryl sulfate (NaDS)) or cationic (trimethyl(tetradecyl) ammonium bromide (TTAB)) surfactants. Fluid flow profiles in a stabilised free liquid film were measured by micron-resolution particle image velocimetry (μ-PIV) combined with a confocal laser scanning microscopy (CLSM) setup. Numerical simulations of electroosmotic flow in the same system were performed using the Finite Element Method. The computational geometry was generated by CLSM. A reasonably good agreement was found between the computed and experimentally measured velocity profiles. The features of the flow profiles and the velocity magnitude were mainly determined by the type of surfactant used. Irrespective of the surfactants used, electroosmotic flow dominated in the midfilm region, where the film is thinnest, while backflow due to pressure build-up developed near the glass rods, where the film is thickest.

Keywords: free liquid film; electroosmotic flow; electrophoresis; electrokinetic; Plateau border

1. Introduction

Liquid foams have a wide range of applications in cosmetics, mining, food, and firefighting. Foam is a multiphase colloidal system made from entrapment of gas in a continuous liquid phase. Drainage refers to gravity- and/or capillary-driven flow of liquid between the gas bubbles through Plateau borders, nodes, and films, and is well documented [1–3]. Plateau borders in foams have higher liquid content, and a free liquid film (~180 μm thick) can be used to model the electrokinetic flow inside Plateau borders. However, manipulation of fluid through a foam system by an external electric field (electrokinetic flow) is still to be understood [4]. For this purpose, an electrokinetic flow in a free liquid film is considered below. The free liquid film is formed by suspending a thin liquid film stabilised by surfactants within a solid frame. The properties of surfactant molecules are described by equilibrium adsorption and adsorption kinetics [5]. The adsorption of ionic surfactant molecules at the gas–liquid and solid–liquid interfaces governs the respective values of the zeta potential [6]. Recently, the authors used a free liquid film to model electrokinetic flow within a foam system [7]. In the past few years, several publications have reported fluid flow in a free liquid film using different procedures [8–16]. A liquid film motor [8–13] has been reported, where a thin, freely suspended liquid film placed between two capacitor plates under a DC power source resulted in a complex motion of the fluid due to uneven charge distribution across the film. In [14,15], film stability was improved by

electroosmotic flow counterbalancing the drainage of a soap bubble [14] and a free liquid film [15]. More recently, an experimental procedure for measuring electroosmotic flow in free liquid film was reported [16]. The authors found [16] that the fluid flow varied depthwise within the free liquid film and developed a CFD (computational fluid dynamic) model to fit the experimental result. Given the complexity of the film structure, the model oversimplified the free liquid film geometry, and, as a result, the fit was not satisfactory [16]. The aim below is (i) to develop an accurate free liquid film geometry using depthwise scanning of the flow cell using confocal laser scanning microscopy (CLSM); (ii) use an accurate film geometry to develop a CFD model for electrokinetic flow in the free liquid film geometry; and (iii) to study the effect of surfactant type on the flow profiles.

2. Materials and Methods

2.1. Solution Preparation

Test solutions were prepared by mixing 50 g of Milli-Q water (15 MΩ·cm deionised water) with glycerol (Sigma-Aldrich, Dorset, UK) and 200 µL of 1 M phosphate buffer solution (Sigma-Aldrich, UK) to adjust the bulk solution molarity to 2 mM. Two solutions were created by placing 50 g of the bulk solution in two beakers and adding 118.2 mg of anionic surfactant sodium lauryl sulfate (NaDS) in one and 89.3 mg of cationic surfactant trimethyl(tetradecyl)ammonium bromide (TTAB) in the other test solution. The concentrations of the two surfactants were just above the critical micelle concentration (CMC). For flow visualisation experiments, 2 µm fluorescent carboxylate-modified polystyrene particles (Sigma-Aldrich) were added to each test solution at a concentration of 0.003%. The electrical conductivities of the test solutions containing TTAB and NaDS was measured as 80.0 $\mu S \cdot cm^{-1}$ and 100.1 $\mu S \cdot cm^{-1}$, respectively. The final pH of both test solutions was recorded as 7.25. Both conductivity and pH were measured using a Thermo Scientific Orion Star A215. The viscosity and refractive index of the test solutions were measured as 4.01×10^{-3} Pa·s and 1.3328, respectively.

2.2. Experimental Setup

A free liquid film holder for electrokinetic flow investigation was made by joining two borosilicate glass rods with an internal diameter of 3 mm and platinised (Pt) titanium rods with a diameter of 2 mm (Ti-shop, William Gregor, London, UK) as shown in Figure 1a. The rods were fixed in the frame holder in such a way as to create a gap of 7.5 mm × 1.4 mm in the middle where the free liquid film was to be suspended.

Before each experiment, the film holder was carefully cleaned to remove contaminants. First, the frame was prepared for the experiments by introducing the test solution onto the frame, and any excess liquid held on the frame was completely removed with a quick burst of compressed air. This procedure was adopted to get all solid surfaces covered by an adsorbed layer of surfactants under investigation. After this, a free liquid film was formed within the gap of the rods by placing ~9 µL of the test solution using a micropipette (Eppendorf, Hamburg, Germany) in the cavity of the frame and gently moving it across to the other end. The free liquid film generated here is in direct contact with the parallel Pt electrode rods and connecting glass rods as shown in Figure 1b. The top and the bottom interfaces of the free liquid film were exposed to air as shown in Figure 1c, and the free liquid film was held in position by surface tension forces. Following the formation of the free liquid film within the film cavity, the device was carefully transferred onto the microscope stage (Figure 1d), and the electrodes were connected to a DC power source (Thurlby Thandar PL30QMD, RS Components Ltd., Corby, UK).

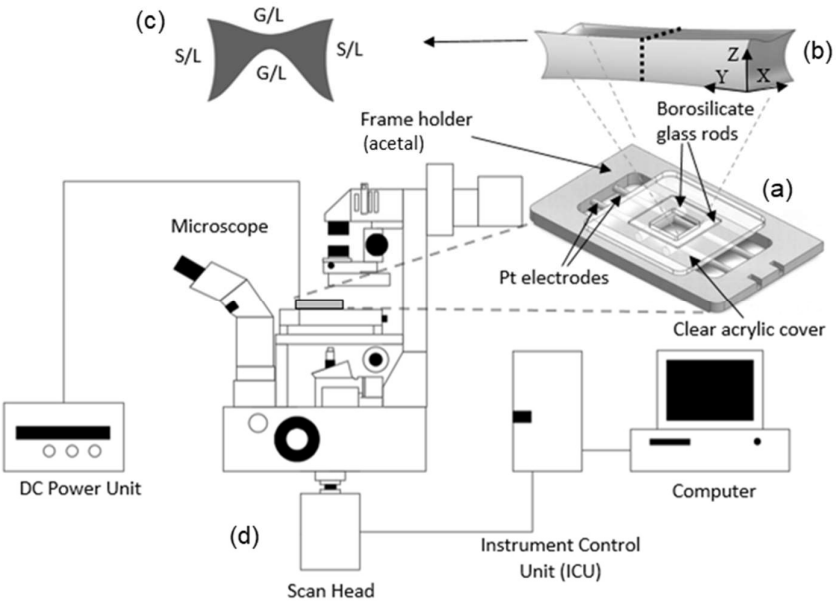

Figure 1. Experimental setup (**a**) free liquid film frame holder; (**b**) free liquid film geometry regenerated for computations; (**c**) a cross section of the free liquid film depicting interfaces: gas–liquid (G/L) interface and solid–liquid (S/L) interface; (**d**) confocal micron-resolution particle image velocimetry (μ-PIV) setup for flow measurements.

2.3. Geometry Measurement of the Free Liquid Film

To measure the film thickness, the following procedure was adopted. First, an electrically neutral dye (rhodamine B) at a concentration of 30 mM was added to each test solution. After that, the free liquid film was scanned using CLSM (Nikon inverted Microscope ECLIPSE TE300 with 20X-0.45NA objective lenses (Tokyo, Japan) and with Bio-Rad RAD200 scan head (Zeiss, Oberkochen, Germany)). The entire length of the film was scanned using 14 locations on the film surface. These 14 locations covered the whole outer surface of the film. At each location, 163 to 326 images were taken from the top surface to the bottom surface of the film with 4 μm distance in the vertical z-direction between successive images. The number of images needed at each location depended on the local film thickness at each position: 163 depthwise images in the thinnest part and 366 depthwise images in the thickest part. Finally, all 14 arrays of images were collated and overlapped in both x and y directions to construct the 3D geometry of the free liquid film using ImageJ software (version 1.51j8, National Institutes of Health, Bethesda, MD, USA) [17]. Film geometry constructed by the above explained method is shown in Figure 2.

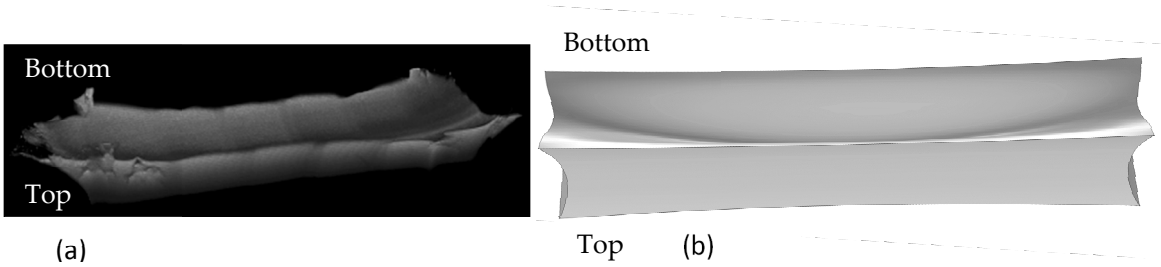

Figure 2. (**a**) Reconstructed image of the free liquid film geometry of trimethyl(tetradecyl) ammonium bromide (TTAB) surfactant from a confocal laser scanning microscope; (**b**) regenerated geometry for computations. Both images are upside down for comparison.

2.4. Flow Visualisation

The velocity field within the free liquid film generated under an external electric field was measured using a CLSM micron-resolution particle image velocimetry (μ-PIV) setup. The system consists of a CLSM scan head, argon-ion laser (wavelength = 488 nm, 100 mJ), photomultiplier tubes (256 × 256 pixels, 8-bit resolution), and a computer with Laser Sharp 2000 software (version 6.0, Zeiss, Oberkochen, Germany) as shown in Figure 1. Fluorescent seed particles (ρ_p = 1005 kg·m^{-3}) of diameter 2 μm with an excitation peak wavelength of 488 nm and emission peak wavelength of 530 nm were used for the flow measurements. Following the identification of top and bottom interfaces of the liquid film using rhodamine B, the flow field was optically scanned at different depths 30 μm apart. For each depth, ten consecutive images were recorded at a frame rate of 2 Hz with a 20X-0.45NA objective lens with a field of view of 690 μm × 690 μm. The optical slice thickness for this setup was estimated to be ~8.4 μm using Cytodex® 3 microcarrier beads (Sigma-Aldrich) suspended in a 30 mM fluorescein isothiocyanate solution. Recorded images were stored in the computer and analysed using software—PIVlab 1.4 and Matlab™ (Natick, MA, USA) [18]. Cross-correlation analysis was performed by selecting 32 pixels × 32 pixels interrogation windows with 50% overlap to obtain a spatial resolution of 20 μm × 20 μm × 8.4 μm. The PIV window analysed was 3200 μm to 3884 μm away from the cathode electrode, as shown in Figure 3.

Figure 3. (**a**) Plan view: PIV window is 3200 μm to 3884 μm away from the cathode electrode; (**b**) end elevation: locations where depthwise velocity profiles in the y-direction (v_y) were measured.

The free liquid film holder used in the experiments was made by joining two borosilicate glass rods. Therefore, it was necessary to measure the zeta potential at the solid–liquid (glass-test solution) interface. For this purpose, ground glass beads made of the same material as the glass rods were used. These glass beads were mixed with each test solution, and the zeta potential was measured by using a Malvern Zetasizer Zs (Malvern Instruments, Malvern, UK). The zeta potential of the latex flow visualisation particles was measured using a DelsaNano HC Particle Analyser (Beckman Coulter, High Wycombe, UK) to estimate the electrophoretic velocity.

2.5. CFD Model

The electric field inside the free liquid film due to external electric potential was determined by Laplace's equation:

$$\boldsymbol{E} = -\nabla\phi \tag{1}$$

$$\nabla\cdot(\epsilon_0\epsilon_r\boldsymbol{E}) = 0 \tag{2}$$

where ϕ is the electric potential, $\boldsymbol{E}$ is the electric field, ϵ_0 is the absolute permittivity of vacuum, ϵ_r is the permittivity of the test fluid. The space charge density is zero within the bulk of the film, because the electroneutrality condition holds outside the electrical double layers. The boundary conditions are (i) electric potential at the liquid–electrode interface, i.e., ϕ = 12 V and ϕ = 0 V (ground electrode); and (ii) zero electric charge at the glass–liquid and solid–liquid interfaces. Since the charge at the surfactant-covered interfaces is balanced by counter-ions from the solution, the net electric charge at the interface is zero. According to Equation (2) and Condition (ii), the electric normal stresses at the gas–liquid interface are equal to zero. Hence, the deformation of the gas–liquid interfaces in the

normal direction was negligible. Preliminary observations confirmed no measurable changes to the film geometry upon application of an external electric field.

The governing equations for the fluid flow are continuity and incompressible Navier–Stokes equations for laminar flow (Stokes flow):

$$\nabla\cdot\left[-pI+\eta(\nabla\boldsymbol{u})^T\right]=0 \tag{3}$$

$$\nabla\cdot\boldsymbol{u}=0 \tag{4}$$

where p is the pressure, $\boldsymbol{u}$ is the velocity vector, η is the dynamic viscosity, and I is the identity tensor. The boundary conditions at the gas–liquid interfaces (top and bottom surfaces open to air) and solid–liquid interfaces (sides of the film in contact with the glass rods) covered with surfactants were set as slip boundaries. The slip velocities, $\boldsymbol{u}_{G/L}$ (gas–liquid) and $\boldsymbol{u}_{S/L}$ (solid–liquid) were determined according to the Helmholtz–Smoluchowski relationship [19] given by the following equation:

$$\boldsymbol{u}_{G/L}=-\varepsilon\psi_0\boldsymbol{E}/\eta;\ \boldsymbol{u}_{S/L}=-\varepsilon\beta_0\boldsymbol{E}/\eta \tag{5}$$

where ε is the solution permittivity, ψ_0 is the zeta potential at the surfactant-covered gas–liquid interface, and β_0 is the zeta potential at the surfactant-covered solid–liquid interface. The no-slip velocity boundary condition was used at the electrodes. Note that the zeta potentials at the gas–liquid interface (ψ_0) and solid–liquid interface (β_0) are different; hence, slip velocities calculated according to Equation (5) are different at the G/L and S/L interfaces. The electrical double layer (EDL) thickness for the experiments was estimated to be 4 nm; hence, the Helmholtz–Smoluchowski relationship [20] is applicable here. The gas–liquid interfaces were tangentially immobile as they were completely covered with surfactants at concentrations at or above CMC [21]. However, the charge on the EDL depends on the type of surfactant used only. All boundary conditions used are shown in Figure 4.

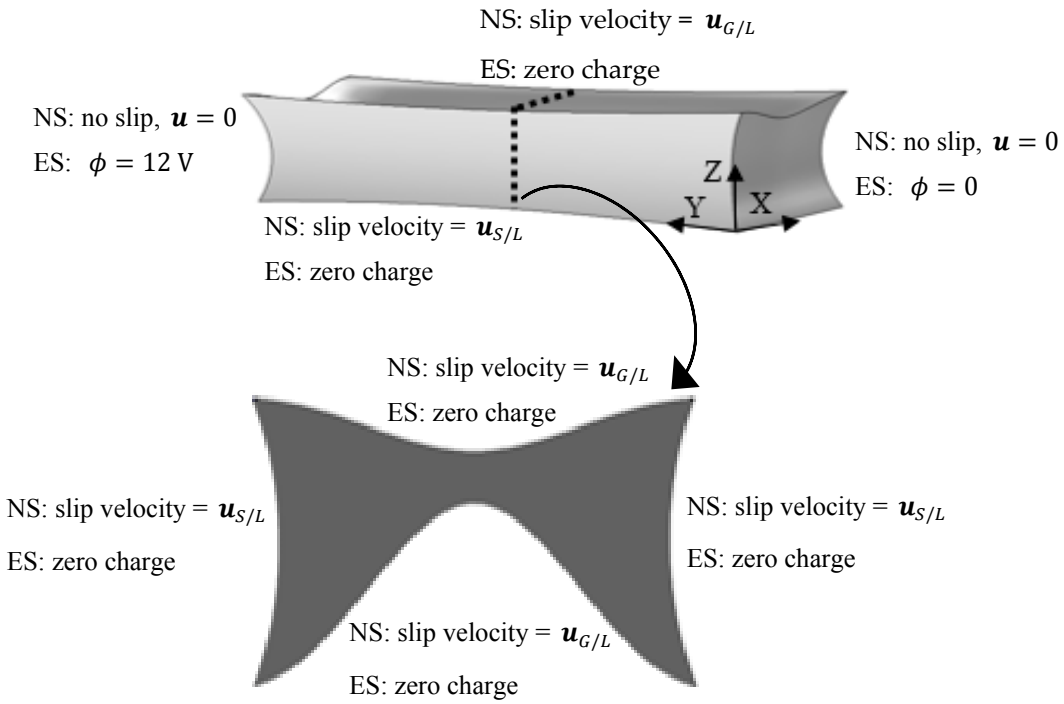

Figure 4. Boundary conditions used for the numerical simulations (NS: Navier–Stokes, ES: Electrostatics).

The measured zeta potentials of the glass particles in TTAB and NaDS solutions were 21 ± 2 mV and -29 ± 3 mV, respectively. The zeta potential at the gas–liquid interface for NaDS at CMC is

−70 mV for pH 7 [6]. The adsorptions of NaDS and TTAB on the interface are 8.91 × 10^{-6} mol·m^{-2} and 1.03 × 10^{-5} mol·m^{-2}, respectively [5], which is very close. Therefore, since the adsorptions are very similar, the zeta potential of TTAB was assumed to be the same value as that of NaDS, but the opposite sign; that is, 70 mV. These values were used to calculate the slip velocities ($\boldsymbol{u}_{G/L}$, $\boldsymbol{u}_{S/L}$) according to Equation (5).

Numerical simulations were performed using the Galerkin Finite Element Method (FEM) in Comsol Multiphysics™ 5.0 (Stockholm, Sweden). The 3D computational geometry generated by CLSM was imported to the Comsol interface and discretised using tetrahedral mesh elements. Equations (1)–(4) were solved simultaneously with relevant boundary conditions for a steady-state solution. Mesh-independency of the solution was confirmed using a higher mesh density of 432,056 elements. The number of degrees of freedom (DOFs) solved was 2,957,700. The computational time was approximately 2 h on an Intel Core i5 64-bit 2.7 GHz processor for each case.

3. Results and Discussion

Preliminary experiments were carried out to identify a range of suitable electric field strengths for electrokinetic flow experiments by changing the voltage from 2 through to 35 V, which corresponds to electric field strengths of 254–4450 V·m^{-1}. It was found that a voltage of 12 V was best suited for the system as higher voltages resulted in substantial electrolysis causing flow disruption while lower voltages did not provide enough driving force for consistent flow. The ionic strength of the system was 5 mM, and the Debye length was estimated to be 4 nm [16].

The experimentally measured velocity from the µ-PIV analysis contained electroosmotic flow in the free liquid film, electrophoresis of tracer particles, pressure-driven flow, and Brownian motion of the tracer particles. For low-Reynolds-number flows, as in the case under investigation here, the resultant velocity was assumed to be a linear superposition of its components expressed as [22]

$$\boldsymbol{u}_m = \boldsymbol{u}_P + \boldsymbol{u}_{EOF}(\psi_0, \beta_0) + \boldsymbol{u}_{EP}(\zeta_p) + \frac{\boldsymbol{d}_{bm}}{\Delta t} \tag{6}$$

where $\boldsymbol{u}_m$ is the measured particle velocity, $\boldsymbol{u}_P$ is the velocity due to pressure, $\boldsymbol{u}_{EOF}$ is the velocity due to electroosmosis, $\boldsymbol{u}_{EP}$ is the particle electrophoretic velocity, and $\boldsymbol{d}_{bm}$ is the displacement vector due to Brownian motion during the observation period Δt. The particle electrophoretic velocity, $\boldsymbol{u}_{EP}$, is a function of zeta potential at the seed particle surface (ζ_p) and the velocity due to electroosmosis; $\boldsymbol{u}_{EOF}$, is a function of zeta potential at the solid–liquid (β_0) and gas–liquid (ψ_0) interfaces. For 2 µm seeding particles, contribution due to Brownian motion can be neglected. Since the electrophoretic mobility of the particles can be measured separately, fluid velocity in the film can be calculated using the following equation:

$$\boldsymbol{u}_f = \boldsymbol{u}_m - \boldsymbol{u}_{EP}(\zeta_p) \tag{7}$$

where $\boldsymbol{u}_f$ is the combined fluid velocity (due to electroosmotic flow ($\boldsymbol{u}_{EOF}$) and the flow caused by pressure gradient ($\boldsymbol{u}_P$) expressed as

$$\boldsymbol{u}_f = \boldsymbol{u}_{EOF}(\psi_0, \beta_0) + \boldsymbol{u}_P \tag{8}$$

The following relationship gives the electrophoretic mobility of a spherical tracer particle with a uniform zeta potential [20]:

$$\mu_{EP} = \frac{2\varepsilon\zeta_p}{3\eta} \tag{9}$$

The latter equation is valid for the case when the EDL is much thinner than the particle radius, which is the case under the experimental conditions used. Even though ε and η can vary within the flow domain, particularly near the interfaces, material properties were assumed to be constant throughout the film. The measured zeta potentials of the fluorescent tracer particles used in the experiments for TTAB and NaDS were 22 ± 4 mV and −31 ± 2 mV, respectively. The corresponding electrophoretic

mobilities determined using Equation (9) for TTAB and NaDS were 1.40×10^{-9} $m^2 \cdot V^{-1} \cdot s^{-1}$ and -1.97×10^{-9} $m^2 \cdot V^{-1} \cdot s^{-1}$, respectively. The resulting electrophoretic drift velocity is given by

$$\mathbf{u}_{EP}(\zeta_p) = \mu_{EP}\mathbf{E} \tag{10}$$

where the electric field ($\mathbf{E}$) was determined from numerical simulations. The fluid velocity due to electroosmotic flow and pressure build-up was obtained using Equation (7) by subtracting the contribution from electrophoretic particle velocity calculated from Equation (10).

To compute the flow field using the FEM in [16], it was assumed that the geometry of the free liquid film was symmetrical about the middepth plane (xy plane, $z = 0$). However, for the case under consideration, the length of the film is 7.5 mm long in the y-direction (Figure 2b), and is hence larger than the capillary length, $\sqrt{\frac{\gamma}{\rho g}} < 2$ mm, where γ ~36 dyn/cm is the liquid/air interfacial tension, ρ is density of water, and g is the gravity acceleration. This means that the gravitational action along the flow cell cannot be neglected. Hence, the liquid film is not completely symmetrical, and this asymmetry should be taken into account in this study for an accurate prediction of the flow field.

The velocity profiles within the free liquid film under an applied electric field were determined from CFD simulations. Figure 5 shows x, y, and z components of the electric field for the $z = 0$ plane due to the applied electric potential difference. It was found that the resultant electric field is uniform and predominantly strong in the y-direction within the PIV window. This observation not only simplifies the PIV analysis but also allows particles to remain in the same depth plane unless carried by pressure flow in the y-direction.

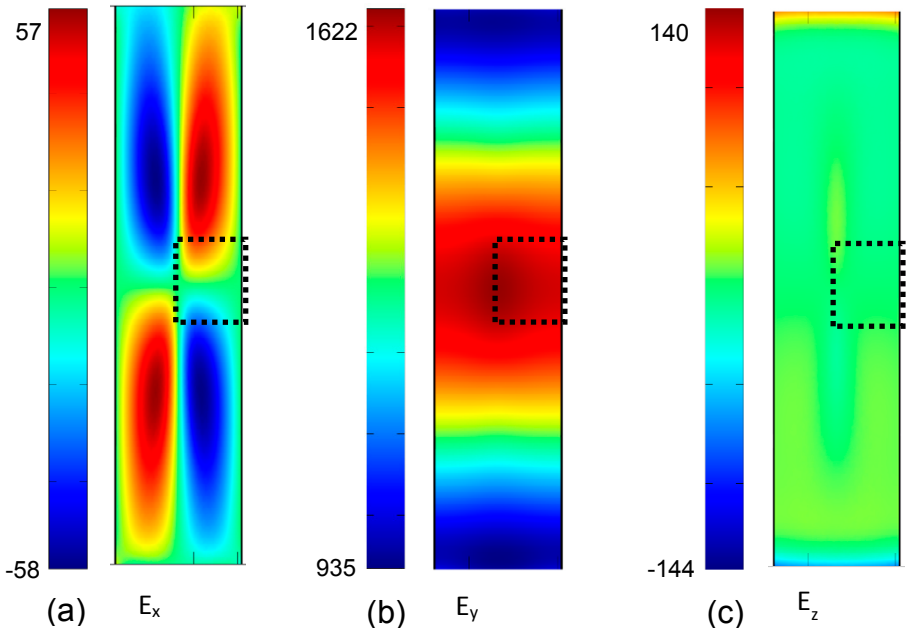

Figure 5. Computational components of the electric field ($V \cdot m^{-1}$) for depthwise plane $z = 0$. (**a**) E_x; (**b**) E_y; (**c**) E_z. The dotted square indicates the μ-PIV window, where experimental velocity measurements were taken.

The computed electric field for a cross section of the liquid film (on xz plane) in the midfilm region is shown in Figure 6. This profile was used in calculating the electrophoretic velocity of seed particles according to Equation (10). The simulated electric field shows ~3 percent variation of the electric field strength from the centre to the glass walls (Figure 6). Additionally, Table 1 shows a significant variation of the free liquid film thickness, h_{min} (Figure 6), for a relatively small variation of the total liquid volume of the film. According to Table 2, our experimental measurements demonstrate that

evaporation causes a small but noticeable influence on the liquid film volume over time. The recorded changes in weight of the free liquid film were about 5–10 percent after 5 min of forming the film. Therefore, during the flow visualisation experiments, a noticeable change in film thickness can be expected. This could lead to a discrepancy between measured values and computed values of velocity within the film.

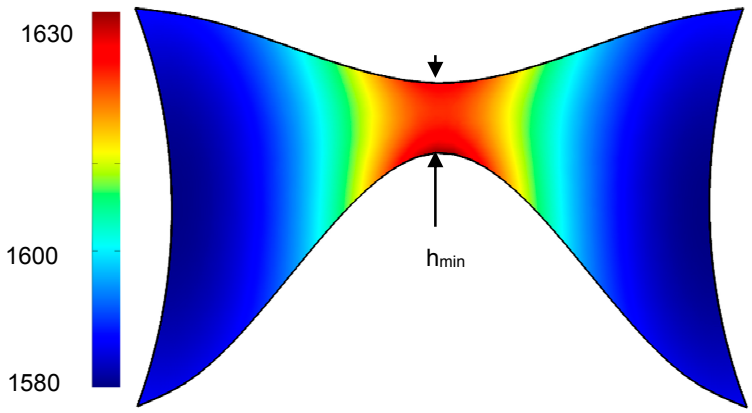

Figure 6. Simulated electric field ($V \cdot m^{-1}$) in the y-direction (E_y).

Table 1. A comparison of different minimum (h_{min}) free liquid thickness variation with respective volume. The film thickness (h_{min}) used in the simulation reference case is 180 µm.

h_{min} (µm)	Volume (μm^3)	% Thickness	% Volume
150	7.10	−16.67	−1.49
180	7.21	0	0
200	7.28	11.11	0.93
220	7.35	22.22	1.89
240	7.42	33.33	2.86

Table 2. Measurement of the free liquid film weight over 5 min.

t (min)	Weight (mg)	SD (mg)
0	10.20	0.26
5	9.43	0.35
Percentage change (%)	8.13	

Figure 7 presents normalised experimental and simulated depthwise velocity profiles in the y-direction ($v_y / v_{y,max}$) for cationic and anionic surfactant free liquid films across seven depth levels in the z-axis. The results were obtained by time averaging the electroosmotic velocity within the PIV window shown in Figure 5. The normalisation value was based on the maximum velocity in the y-direction for NaDS and the minimum velocity in the y-direction for TTAB at the centre of the film. The simulation maximum and minimum velocities for NaDS surfactant free liquid film were 19.8 $\mu m \cdot s^{-1}$ and -20.2 $\mu m \cdot s^{-1}$, respectively, while the experimental minimum and maximum velocities were 23.7 $\mu m \cdot s^{-1}$ and -20.3 $\mu m \cdot s^{-1}$, respectively, which are relatively close. The simulated minimum and maximum velocities of the free liquid film with TTAB surfactant were -19.8 $\mu m \cdot s^{-1}$ and 20.2 $\mu m \cdot s^{-1}$, respectively. The measured experimental minimum and maximum velocities were 8.7 $\mu m \cdot s^{-1}$ and -12.0 $\mu m \cdot s^{-1}$, correspondingly. The mismatch in experimental and simulated velocities for TTAB surfactant is much greater compared with the NaDS surfactant comparison. Note that the zeta potential value for NaDS solutions was chosen according to [6], while the value of zeta potential in the case of TTAB was selected based on the analogy described above, which is not necessarily

true. For this reason, we repeated the numerical simulation for TTAB using a lower gas–liquid interface zeta potential of 30 mV. The simulation minimum and maximum velocities were -6.3 μm·s^{-1} and 8.0 μm·s^{-1}. These values are significantly closer to the experimental values -12.0 μm·s^{-1} and 8.7 μm·s^{-1}, correspondingly. The latter suggests that the zeta potential could be lower than the 70 mV that was used initially. Note that in the case of zeta potential equal to 30 mV, the agreement between computed and measured profiles also improved (Figure 7c).

Further simulations were performed using different minimum film thicknesses from 150 μm to 240 μm to understand the effect of film thickness variation on the velocity profiles as shown in Figure 8. The normalised fluid velocity profiles in the y-direction ($v_y/v_{y,max}$) for each geometry at the middepth plane (z = 0) were compared with the corresponding experimental dataset for both surfactant types. In both cases, the computed values from CFD showed that a thicker free liquid film (~200 μm) had a better velocity fitting to the experimental data compared to the thickness used (180 μm). This finding suggests that the thickness measurements taken here have been underestimating the true thickness of the film.

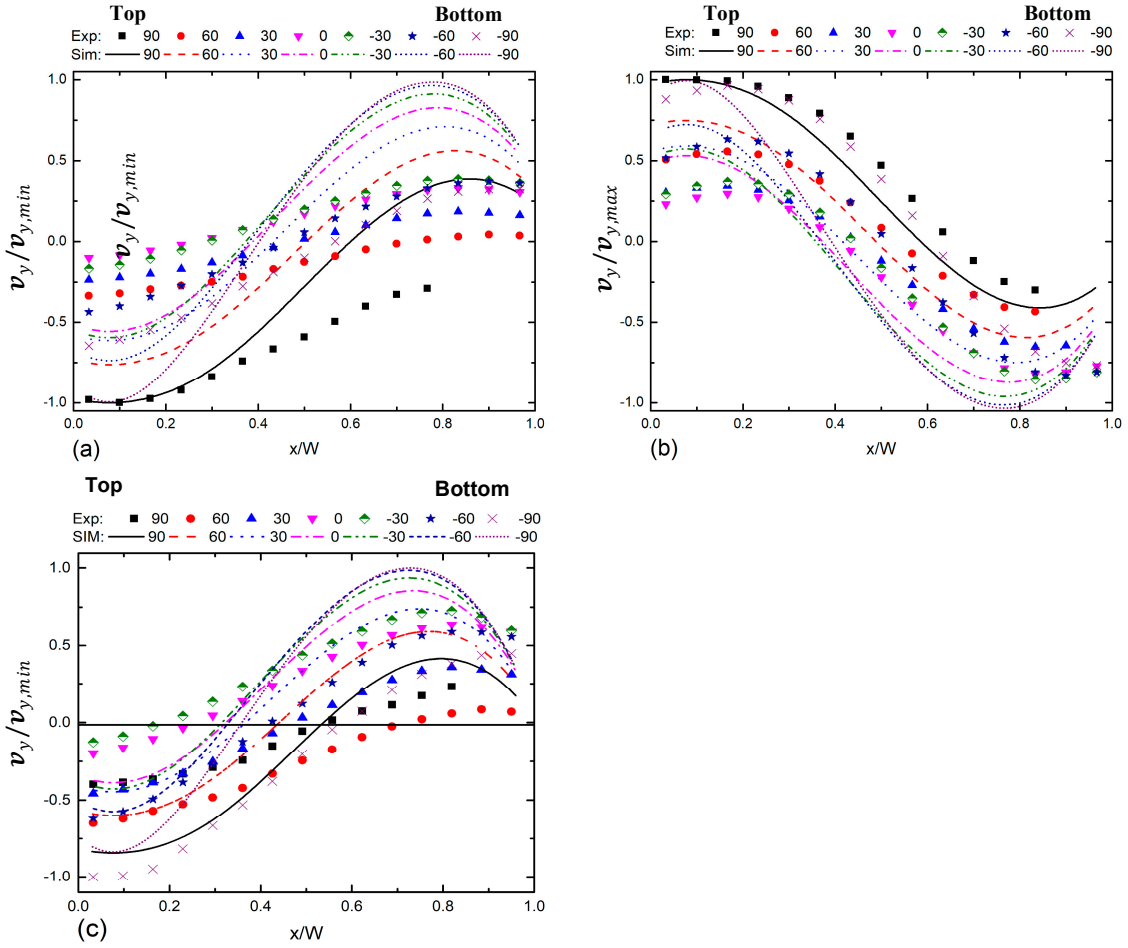

Figure 7. Experimental and computational fluid dynamic (CFD) depthwise resultant velocity in the y-direction ($v_y/v_{y,max}$) due to electroosmotic and pressure flow for (**a**) TTAB using a zeta potential value of 70 mV and (**b**) NaDS using a zeta potential value of -70 mV; (**c**) TTAB using a zeta potential value of 30 mV. The results are for time-averaged velocity in the y-direction within the PIV window. The dataset shows half of the free liquid film, where distance measured from the centre of the film (x) was normalised by half film width (w).

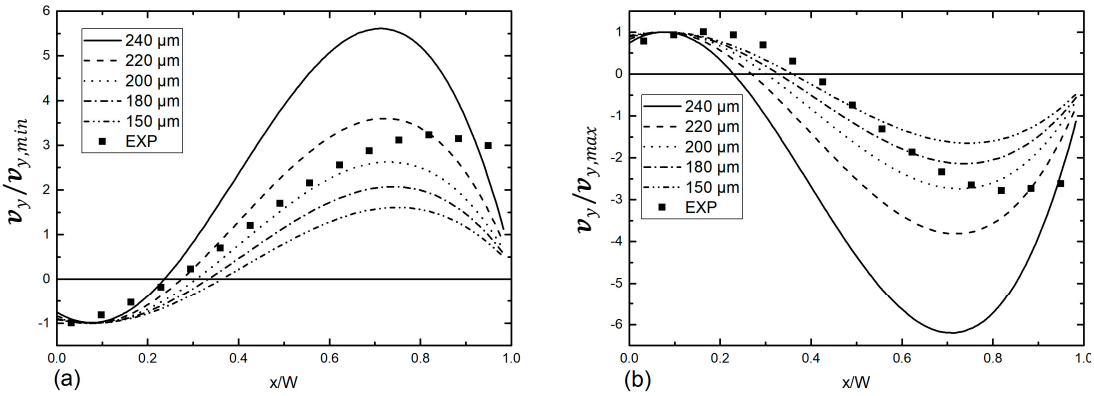

Figure 8. Normalised fluid velocity profiles in the y-direction ($v_y/v_{y,max}$) at $z = 0$ plane for different minimum film thicknesses for numerical simulations and experimental (EXP) results (**a**) for TTAB and (**b**) for NaDS. Zeta potentials used here are −70 mV and 70 mV for NaDS and TTAB, respectively.

It is important to consider surfactant adsorption at the solid–liquid and gas–liquid interfaces to understand the obtained results. The adsorption of surfactant molecules on a solid–liquid interface depends on the nature of the surfactant and the nature of the solid surface [23]. The two surfactants used in this system is reported to show a four-region adsorption isotherm against oppositely charged substrates [23] as the concentration of surfactant increases. In Region I, surfactant monomers are electrostatically adsorbed to the substrate at low concentration according to Henry's law [24]; in Region II, as the concentration increases, a sharp gain in lateral interaction between the adsorbed monomers can be observed, leading to surfactant aggregation at the interface; in Region III, there is a decreased rate of adsorption; and in Region IV, the adsorption rate stops above the CMC [25].

For the case of TTAB, the cationic surfactant gets adsorbed to the borosilicate glass rods and the latex particles (both negatively charged) firstly by the electrostatic attraction, which follows the Schulze–Hardy rule [26] forming hemimicelles. As the concentration of the surfactant increases above the CMC, further surfactant molecules get adsorbed by hydrophobic chain–chain interaction between the adsorbed monolayer [27] as shown in Figure 9a. Furthermore, the adsorption mechanism of the surfactant on silica surfaces is also similar to that on other mineral oxide surfaces, and the zeta potential of the surface will be positive [25]. An anionic surfactant does not adsorb on a negative hydrophilic substrate as electrostatic repulsion does not favour adsorption [25,28]. However, the adsorption kinetics of a surfactant molecule on a hydrophilic surface at pH > 6 is significantly faster and the final adsorbed amount is greater for a cationic surfactant than for an anionic surfactant [23]. The presence of electrolyte improves the adsorption of an anionic surfactant on a negatively charged surface [23,25]. In the current system, a phosphate buffer was used to maintain the solution pH as constant. The adsorption of an anionic surfactant on glass surfaces is poor as shown in Figure 9c in comparison to a cationic surfactant, resulting in a higher concentration of surfactant molecules in the bulk. Nonetheless, the zeta potential at the interface is negative. The adsorption of surfactant molecules in the gas–liquid interface for the case of TTAB is shown in Figure 9b, and the adsorption of NaDS is similar to the case presented.

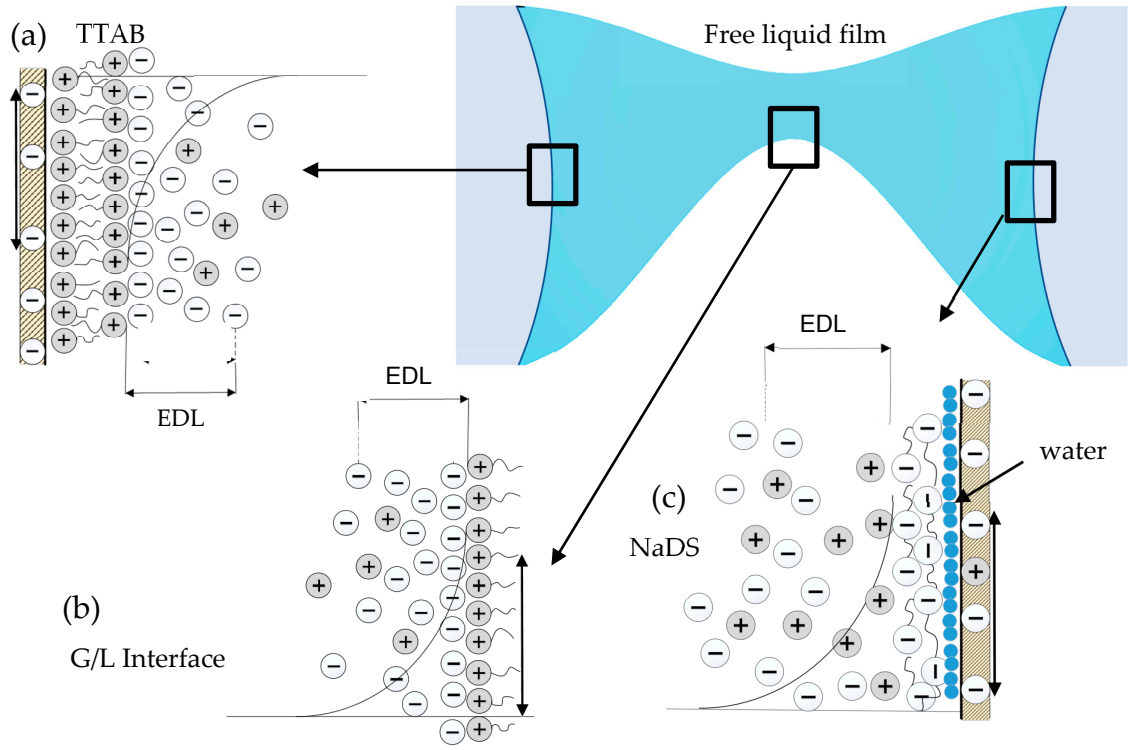

Figure 9. Schematic representation of the surfactant arrangement at the interfaces; case (**a**) TTAB surfactant arrangement at solid–liquid interface and electrical double layer (EDL) formation; case (**b**) TTAB surfactant arrangement at the gas–liquid interfaces and EDL formation; case (**c**) sodium lauryl sulfate (NaDS) surfactant molecules at the solid–liquid interfaces and EDL formation [23,25,29].

Figure 10 shows a comparison of the experimental and the CFD velocity profiles in the y-direction ($v_y/v_{y,max}$) for NaDS and TTAB surfactant for a cross-sectional plane across xz (based on seven depthwise measurement planes). Electroosmotic flow is dominant in the middle of the channel, where the film is thinnest, while backflow is developed near the glass rods, where the free liquid film is thick due to gravitational effects. This creates a symmetrical flow about the yz plane across the middle of the film, but the flow about the xy plane (z = 0) is asymmetrical. Overall, a good agreement was found between the numerically simulated and the experimental results validating the model. In a foam, Plateau borders are oriented at different angles to the gravitational vector; hence, the thickness and shape of these borders will vary considerably. However, this result will be invaluable in understanding electroosmotic flow in such complex geometries, where several Plateau borders meet to make a network of deformable channels.

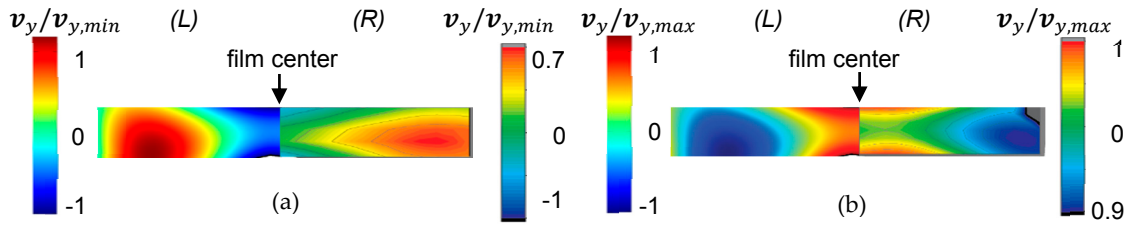

Figure 10. Depthwise flow profiles in the y-direction ($v_y/v_{y,max}$), CFD (L) and experimental (R) within the free liquid film for (**a**) TTAB and (**b**) NaDS.

Each experimental run involved recording seven depthwise flow measurements (different z levels) and took approximately 300 s to complete. During this time, the film thickness was reduced due to

evaporation from the gas–liquid interface as shown in Figure 11. The estimated loss of film thickness is about 10–40 μm at the end of each experimental run. As the liquid evaporates from the interface, capillary action pulling the liquid towards the glass rods can reposition the film vertically causing uncertainty in the depthwise location of the film. This film thickness measurement experiment was performed with the laser light 'on' and 'off' to understand whether the PIV illumination contributes to the film thinning. Film thinning behaviour was found to be similar for both cases, confirming no additional effect from the laser light on evaporation.

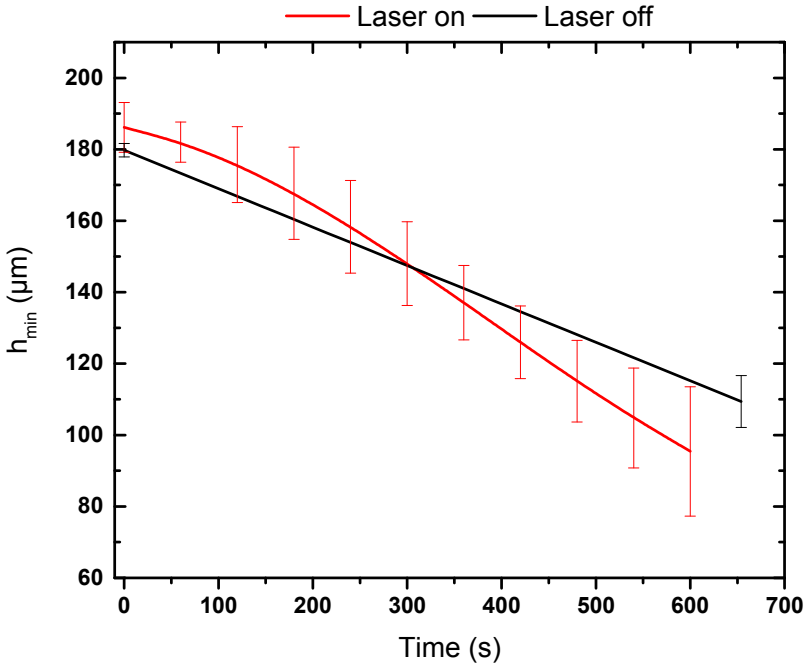

Figure 11. Thickness changes in the free liquid film with time.

4. Conclusions

Electrokinetic flow in a sufficiently thick (180 μm) free liquid film was investigated as a model for understanding of the electrokinetic phenomena in foam Plateau borders made of different surfactants. The free liquid film was stabilised by either anionic (sodium lauryl sulfate (NaDS)) or cationic (trimethyl(tetradecyl) ammonium bromide (TTAB)) surfactant. Fluid flow profiles were measured by micron-resolution particle image velocimetry (μ-PIV) combined with a confocal laser scanning microscopy (CLSM) setup. A numerical simulation of the electroosmotic flow in the same system was also performed using the Finite Element Method to understand the flow dynamics. A reasonably good agreement was found between the numerical simulations and the experimental results, validating the model. Due to gravitational effects and capillary pulling, the free liquid film suspended on the frame formed an asymmetrical geometry about the midhorizontal plane through the film; hence, the computational domain was generated by CLSM. For both surfactant types used, the electroosmotic flow was observed in the mid-film region, where the film is thinnest, while backflow due to pressure build-up developed near the glass rods, where the film is thickest. The agreement between the computational and the experimental results was better in the case of NaDS compared with TTAB, as the gas–liquid zeta potential for TTAB was assumed. Evaporation from the interface caused the film to progressively thin over time and change the shape of the film; hence, these factors should be taken into account for an accurate prediction of flow in deformable channels such as Plateau borders.

Acknowledgments: The authors would like to thank the Department of Chemical Engineering at Loughborough University for a doctoral scholarship for A.H.S.; Marie Curie CoWet project, EU; and MAP EVAPORATION,

European Space Agency. The authors would also like to thank Tony Eyre for technical assistance and Shaghayegh Ghanizadeh, Sameer Chourasia, Hisham Mohamed and Ben Kew for laboratory support.

Author Contributions: A.H.S. and H.C.H.B. conceived and designed the experiments; A.H.S. and A.T. performed the experiments; H.C.H.B., A.H.S. and V.S. analysed the data. All authors contributed in writing the paper.

Conflicts of Interest: The authors declare no conflict of interest.

Abbreviations

μ-PIV	micron-resolution particle image velocimetry
CLSM	confocal laser scanning microscopy
CMC	critical micelle concentration
NaDS	sodium lauryl sulfate (anionic surfactant)
TTAB	trimethyl(tetradecyl)ammonium bromide (cationic surfactant)

References

1. Arjmandi-Tash, O.; Trybala, A.; Mahdi, F.M.; Kovalchuk, N.M.; Starov, V. Foams built up by non-Newtonian polymeric solutions: Free drainage. *Aspects* **2017**, *521*, 112–120. [CrossRef]
2. Bureiko, A.; Arjmandi-Tash, O.; Kovalchuk, N.; Trybala, A.; Starov, V. Interaction of foam with a porous medium: Theory and calculations. *Eur. Phys. J. Spec. Top.* **2015**, *224*, 457–469. [CrossRef]
3. Arjmandi-Tash, O.; Kovalchuk, N.; Trybala, A.; Starov, V. Foam drainage placed on a porous substrate. *Soft Matter* **2015**, *11*, 3643. [CrossRef] [PubMed]
4. Bonhomme, O.; Blanc, B.; Joly, L.; Ybert, C.; Biance, A.-L. Electrokinetic transport in liquid foams. *Adv. Colloid Interface Sci.* **2017**, *247*, 477–490. [CrossRef] [PubMed]
5. Mucic, N.; Javadi, A.; Kovalchuk, N.M.; Aksenenko, E.V.; Miller, R. Dynamics of interfacial layers-Experimental feasibilities of adsorption kinetics and dilational rheology. *Adv. Colloid Interface Sci.* **2011**, *168*, 167–178. [CrossRef] [PubMed]
6. Yoon, R.H.; Yordan, J.L. Zeta-potential measurements on microbubbles generated using various surfactants. *J. Colloid Interface Sci.* **1986**, *113*, 430–438. [CrossRef]
7. Hussein Sheik, A.; Bandulasena, H.C.H.; Starov, V.; Trybala, A. Determining Electroosmotic Velocity in a Free Liquid Film. Presented at the 20th International Conference on Miniaturized Systems for Chemistry and Life Sciences, MicroTAS 2016, Dublin, Ireland, UK, 9–13 October 2016; pp. 766–767.
8. Nasiri, M.; Shirsavar, R.; Saghaei, T.; Ramos, A. Simulation of liquid film motor: A charge induction mechanism. *Microfluid. Nanofluid.* **2015**, *19*, 133–139. [CrossRef]
9. Feiz, M.S.; Namin, R.M.; Amjadi, A. Theory of the liquid film motor. *Phys. Rev. E* **2015**, *92*, 1–9. [CrossRef] [PubMed]
10. Amjadi, A.; Shirsavar, R.; Radja, N.H.; Ejtehadi, M.R. A Liquid Film Motor. *Physics* **2008**, *6*, 9.
11. Liu, Z.Q.; Zhang, G.C.; Li, Y.J.; Jiang, S.R. Water film motor driven by alternating electric fields: Its dynamical characteristics. *Phys. Rev. E* **2012**, *85*, 36314. [CrossRef] [PubMed]
12. Liu, Z.-Q.; Li, Y.-J.; Zhang, G.-C.; Jiang, S.-R. Dynamical mechanism of the liquid film motor. *Phys. Rev. E* **2011**, *83*, 26303. [CrossRef] [PubMed]
13. Amjadi, A.; Nejati, A.; Sobhani, S.O.; Shirsavar, R. Electro/Magnetically Induced Controllable Rotation in Small-scale Liquid Flow. *Phys. Fluid Dyn.* **2013**.
14. Bonhomme, O.; Liot, O.; Biance, A.-L.; Bocquet, L. Soft Nanofluidic Transport in a Soap Film. *Phys. Rev. Lett.* **2013**, *110*, 54502. [CrossRef] [PubMed]
15. Sett, S.; Sahu, R.P.; Sinha-Ray, S.; Yarin, A.L. Experimental Investigation of Eletrokinetic Stabilization of Gravitational Drainage of Ionic Surfactants Films. *Electrochim. Acta* **2016**, *187*, 693–703. [CrossRef]
16. Hussein Sheik, A.; Bandulasena, H.C.H.; Starov, V.; Trybala, A. Electroosmotic flow measurements in a freely suspended liquid film: Experimhents and numerical simulations. *Electrophoresis* **2017**, *38*, 2554–2560. [CrossRef] [PubMed]
17. Preibisch, S.; Saalfeld, S.; Tomancak, P. Globally optimal stitching of tiled 3D microscopic image acquisitions. *Bioinformatics* **2009**, *25*, 1463–1465. [CrossRef] [PubMed]
18. Thielicke, W.; Stamhuis, E.J. PIVlab–Towards User-friendly, Affordable and Accurate Digital Particle Image Velocimetry in MATLAB. *J. Open Res. Softw.* **2014**, *2*. [CrossRef]

19. Baldessari, F.; Santiago, J.G. Electrophoresis in nanochannels: Brief review and speculation. *J. Nanobiotechnol.* **2006**, *4*, 12. [CrossRef] [PubMed]
20. Hunter, R.J.R.J. *Zeta Potential in Colloid Science: Principles and Applications*; Academic Press: London, UK, 1981; ISBN 1483214087.
21. Vassilieff, C.S.; Nickolova, B.N.; Manev, E.D. Thinning of foam films of micellar surfactant solutions Nonionic surfactants C 10 H21(OC2H4)8OH and C12H25(OC2H4)8OH. *Colloid Polym. Sci.* **2008**, *286*, 475–480. [CrossRef]
22. Devasenathipathy, S.; Santiago, J.G.; Takehara, K. Particle tracking techniques for electrokinetic microchannel flows. *Anal. Chem.* **2002**, *74*, 3704–3713. [CrossRef] [PubMed]
23. Paria, S.; Khilar, K.C. A review on experimental studies of surfactant adsorption at the hydrophilic solid–water interface. *Adv. Colloid Interface Sci.* **2004**, *110*, 75–95. [CrossRef] [PubMed]
24. Chandar, P.; Somasundaran, P.; Turrot, N.J. Fluorescence Probe Studies on the Structure of the Adsorbed Layer of Dodecyl Sulfate at the Alumina-Water Interface. *J. Colloid Interface Sci.* **1987**, *117*, 31–46. [CrossRef]
25. Atkin, R.; Craig, V.S.J.; Wanless, E.J.; Biggs, S. Mechanism of cationic surfactant adsorption at the solid–aqueous interface. *Adv. Colloid Interface Sci.* **2003**, *103*, 219–304. [CrossRef]
26. Paria, S.; Manohar, C.; Khilar, K.C. Kinetics of Adsorption of Anionic, Cationic, and Nonionic Surfactants. *Ind. Eng. Chem. Res.* **2005**, *44*, 3091–3098. [CrossRef]
27. Deleurence, R.; Parneix, C.; Monteux, C. Cecile Monteux Mixtures of latex particles and the surfactant of opposite charge used as interface stabilizers—Influence of particle contact angle, zeta potential, flocculation and shear energy. *Soft Matter* **2014**, *10*, 7088–7095. [CrossRef] [PubMed]
28. Penta, N.K.; Amanapu, H.P.; Peethala, B.C.; Babu, S.V. Use of anionic surfactants for selective polishing of silicon dioxide over silicon nitride films using colloidal silica-based slurries. *Appl. Surf. Sci.* **2013**, *283*, 986–992. [CrossRef]
29. Szymczyk, K.; Zdziennicka, A.; Ja, B. Adsorption and wetting properties of cationic, anionic and nonionic surfactants in the glass-aqueous solution of surfactant-air system. *Mater. Chem. Phys.* **2015**, *162*, 166–176. [CrossRef]